Tailoring C_{60} for Efficient Inorganic $CsPbI_2Br$ Perovskite Solar Cells and Modules

Chong Liu, Yuzhao Yang, Cuiling Zhang, Shaohang Wu, Liyu Wei, Fei Guo, Gowri Manohari Arumugam, Jinlong Hu, Xingyuan Liu, Jie Lin, Ruud E. I. Schropp, and Yaohua Mai**

Although inorganic perovskite solar cells (PSCs) are promising in thermal stability, their large open-circuit voltage (V_{OC}) deficit and difficulty in large-area preparation still limit their development toward commercialization. The present work tailors C_{60} via a codoping strategy to construct an efficient electron-transporting layer (ETL), leading to a significant improvement in V_{OC} of the inverted inorganic $CsPbI_2Br$ PSC. Specifically, tris(pentafluorophenyl)borane (TPFPB) is introduced as a dopant to lower the lowest unoccupied molecular orbital (LUMO) level of the C_{60} layer by forming a Lewis acidic adduct. The enlarged free energy difference provides a favorable enhancement in electron injection and thereby reduces charge recombination. Subsequently, a nonhygroscopic lithium salt ($LiClO_4$) is added to increase electron mobility and conductivity of the film, leading to a reduction in the device hysteresis and facilitating the fabrication of a large-area device. Finally, the as-optimized inorganic $CsPbI_2Br$ PSCs gain a champion power conversion efficiency (PCE) of 15.19%, with a stabilized power output (SPO) of 14.21% (0.09 cm^2). More importantly, this work also demonstrates a record PCE of 14.44% for large-area inorganic $CsPbI_2Br$ PSCs (1.0 cm^2) and reports the first inorganic perovskite solar module with the excellent efficiency exceeding 12% (10.92 cm^2) by a self-developed quasi-curved heating method.

The open-circuit voltage deficits (E_g/q-V_{OC}) of the state-of-the-art organic–inorganic hybrid perovskite solar cell (PSCs) have been minimized to the level of ≈0.3 V,[1] which is comparable with the industrial crystalline silicon (c-Si) solar cells,[2] leading to the realization of certified power conversion efficiency (PCE) up to 25.2% within a relatively short period of time.[3–8] At the same time, increasing attention has been paid to the drawbacks of organic–inorganic hybrid PSCs, such as stability,[9] toxicity,[10] and scalability.[11,12] As a potential solution to address the thermal instability issue of organic–inorganic hybrid PSCs,[13–15] the inorganic counterparts have gained a rapid development in the past several years.[13–26] Among them, $CsPbI_3$ owns the most appropriate bandgap (E_g = 1.73 eV) but suffers from unstable structure, while $CsPbBr_3$ has superior stability but has a large bandgap (E_g = 2.3 eV). $CsPbI_2Br$, with the bandgap of 1.92 eV, is regarded as the best compromise after comprehensively balancing the trade-off between bandgap and structural stability.[15] Nevertheless, according to a statistic of PCE as a function of V_{OC}, the large V_{OC} deficit still limits a further improvement in PCE of inorganic $CsPbI_2Br$ PSCs, especially for the inverted architecture (Figure S1a and Table S1, Supporting Information).[27–31] In addition, a severe decline in PCE will happen when the cell areas are scaled up (Figure S1b, Supporting Information),[30–34] which can be ascribed to the deteriorating quality and uniformity of the perovskite film. Consequently, the high efficient large-area inorganic PSCs is a challenge, let alone the inorganic perovskite solar modules. As far as we known, no inorganic perovskite solar modules have been reported so far.

In general, the V_{OC} deficits in the PSCs are mainly ascribed to leakage loss in bulk films, trap states at interfaces, and mismatched band alignment. Several approaches including increasing grain size,[23] interface passivation,[1,7] and grain boundary passivation[35] have been applied to address these aforementioned issues. For instances, Yang et al. found that molecules with carboxyl, amine, and aromatic functional groups can interact with perovskite and realize passivation of grain boundaries, leading to the record low V_{OC} deficit of 0.34 V.[1] In addition, the V_{OC} is also determined by the quasi-Fermi level

---

C. Liu, Dr. Y. Yang, C. Zhang, Dr. S. Wu, Prof. F. Guo, Dr. G. M. Arumugam, Dr. J. Hu, Prof. R. E. I. Schropp, Prof. Y. Mai
Institute of New Energy Technology
College of Information Science and Technology
Jinan University
Guangzhou 510632, China
E-mail: yangyuzh@jnu.edu.cn; yaohuamai@jnu.edu.cn

L. Wei
Shenzhen Key Laboratory of Nanobiomechanics
Shenzhen Institutes of Advanced Technology
Chinese Academy of Sciences
Shenzhen 518055, China

Prof. X. Liu, Prof. J. Lin
State Key Laboratory of Luminescence and Applications
Changchun Institute of Optics
Fine Mechanics and Physics
Chinese Academy of Sciences
Changchun 130033, China

The ORCID identification number(s) for the author(s) of this article can be found under https://doi.org/10.1002/adma.201907361.

DOI: 10.1002/adma.201907361

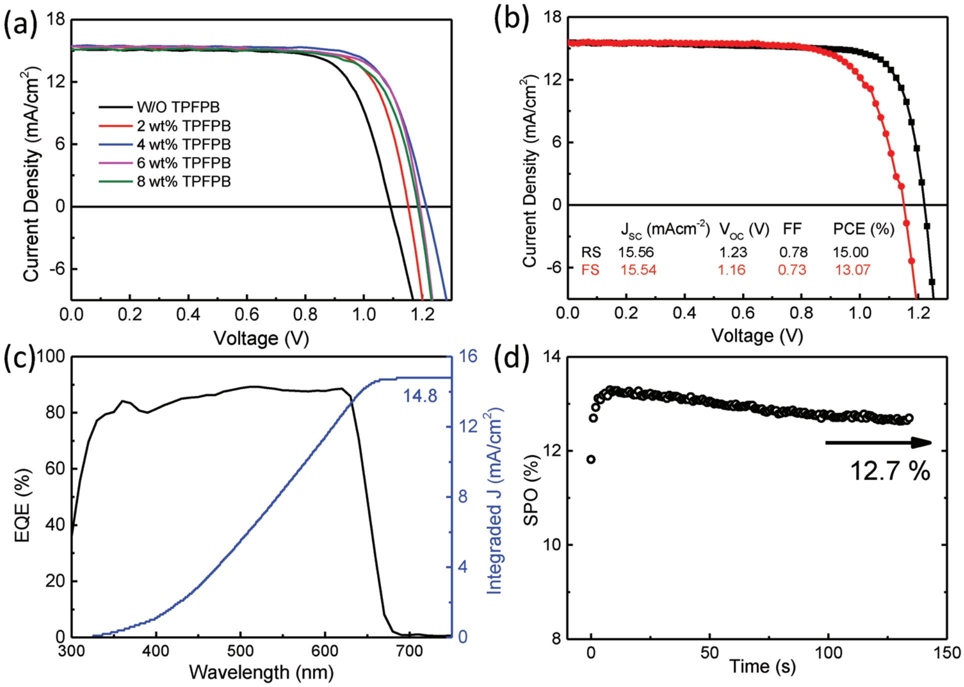

Figure 1. a) Typical *J–V* curves of inorganic $CsPbI_2Br$ PSCs with varying TPFPB dopant concentrations. b) The best performed inorganic $CsPbI_2Br$ PSC obtained at the 4 wt% TPFPB dopant concentration; the scan directions of black line and red line are reverse scan (RS) and forward scan (FS), respectively. c) EQE spectrum and a relevant integrated current density curve. d) SPO as a function of time held at 0.95 V forward bias.

splitting of electrons and holes under illumination. In this respect, obtaining high quality perovskite absorber layers is not the only essential concern, charge transporting layers (CTLs) with suitable energy levels that are highly capable of charge injection are regarded as another essential concern to fabricate high-performance PSCs.[36,37] Recently, we reported an electron transporting bilayer of $ZnO@C_{60}$, which significantly enhanced the V_{OC} of inverted all-inorganic PSCs.[14,30] On the one hand, the ZnO layer (ETL_1) has an aligned conduction band edge but high valence band offsets with the perovskite layer that promotes the splitting of quasi-Fermi levels and prevents holes from flowing to the cathode. On the other hand, the C_{60} layer (ETL_2) with deep LUMO level is favorable to extract electrons from the perovskite/ZnO layers (Figure S2b, Supporting Information).[38,39] Based on these considerations, the electron extraction ability can be further strengthened by tailoring C_{60} to a deeper LUMO level. In general, introducing a dopant with an electron-accepting group may be an effective strategy.[40] The tricoordinated organoboron compound tris(pentafluorophenyl) borane (TPFPB) with a vacant p-orbital of the boron atom is a widely used Lewis acid to coordinate with large π-conjugated carbon skeleton materials in organic solar cells.[41] Recently, Luo and co-workers utilized the TPFPB as a Lewis acidic dopant into the Lewis basic poly[bis(4-phenyl)(2,4,6-trimethylphenyl) amine] (PTAA) hole transporting layer (HTL) in PSCs, which formed a PTAA·TPFPB adduct to enhance hole mobility and shifted its HOMO/LUMO level downward.[42]

In this study, we propose a codoping strategy using TPFPB and $LiClO_4$ to tailor the C_{60} for fabrication of highly efficient inorganic $CsPbI_2Br$ PSCs with lower hysteresis. The optimized inverted inorganic $CsPbI_2Br$ PSCs achieved a champion PCE of 15.19% for a small-area device (0.09 cm^2) with ≈100 mV V_{OC} improvement due to the enhancement of charge extraction and reduction of trap states. Notably, a maximum PCE of 14.44% was obtained for large-area device (1.0 cm^2), which is the highest PCE reported for inorganic $CsPbI_2Br$ PSCs. More importantly, by a self-developed large-area inorganic $CsPbI_2Br$ perovskite film preparation method called quasi-curved heating method, an inorganic perovskite solar module with a prominent PCE beyond 12% was obtained for the first time.

The reference inverted all-inorganic PSCs have a structure of FTO (fluorine-doped tin oxide)/NiO_x/$CsPbI_2Br$/$ZnO@C_{60}$/Ag in our previously published works (Figure S2a, Supporting Information).[14,30] In this work, we innovatively introduced the Lewis acidic dopant of TPFPB into the C_{60} solution and carefully studied the corresponding photovoltaic performances. The typical *J–V* curves and parameters of inorganic $CsPbI_2Br$ PSCs with varying dopant concentrations of TPFPB are represented in **Figure 1**a and Table S2 (Supporting Information), respectively. It can be observed that the V_{OC} is significantly enhanced from 1.09 to 1.21 V with increase in dopant concentration of TPFPB from 0 wt% to 4 wt% and then slightly decreases upon further increase of the dopant concentration from 4 wt% to 8 wt%. The optimized device showed a best performance of PCE of 15.0%, with V_{OC} of 1.23 eV, J_{SC} of 15.56 mA cm^{-2}, and FF of 0.78 for 4 wt% dopant concentration of TPFPB (Figure 1b). Moreover, the external quantum efficiency (EQE) spectrum has been recorded to confirm the accuracy of the J_{SC} obtained from the *J–V* curves (Figure 1c). The integrated J_{SC} was 14.8 mA cm^{-2}, which is fairly close to the value of 15.56 mA cm^{-2} from *J–V* curve (deviation less than 5%). We then performed

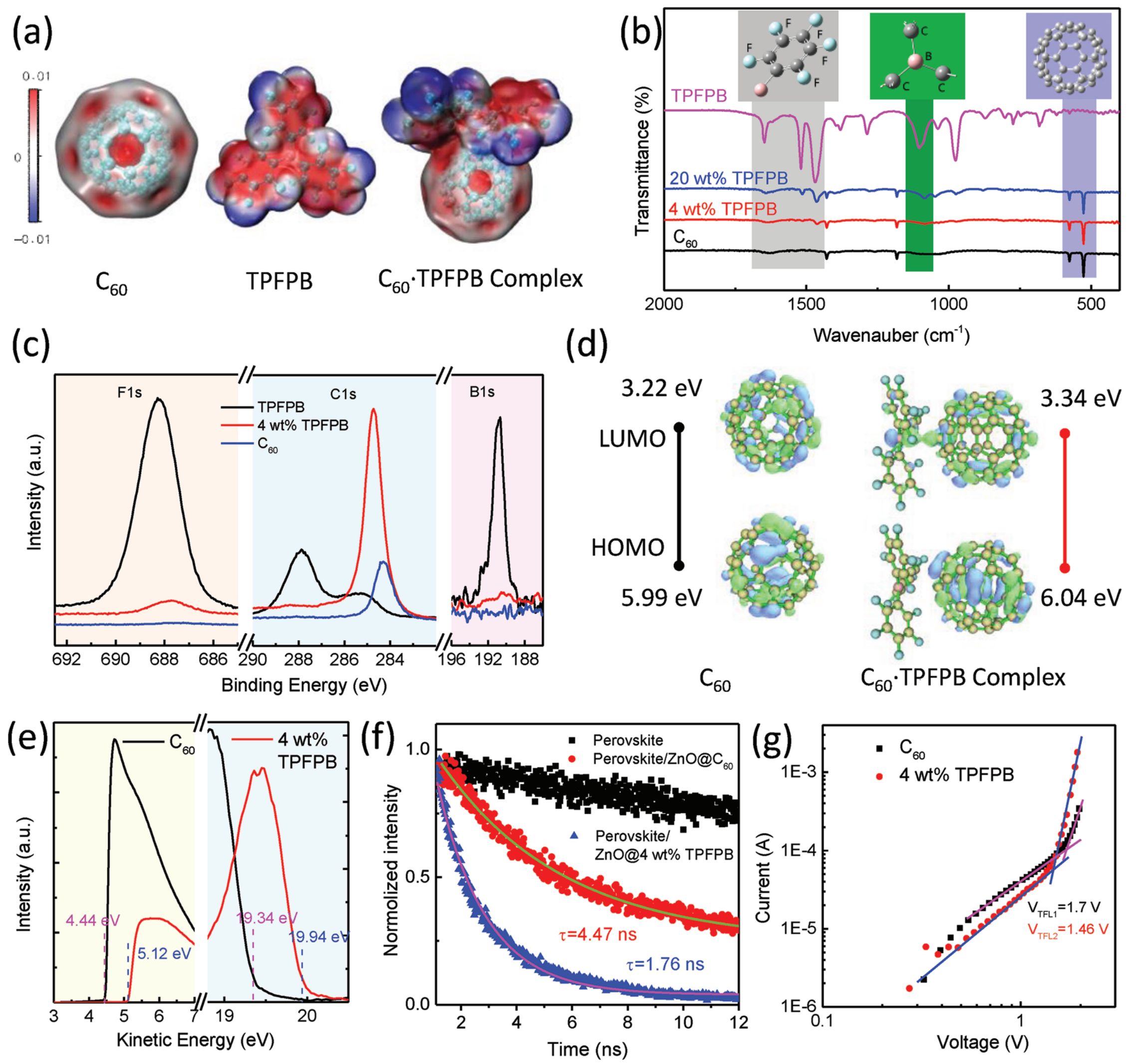

Figure 2. a) The molecular structures and calculated ESP images of C_{60}, TPFPB, and C_{60}·TPFPB complex. b) The FTIR spectra for C_{60}, TPFPB, and TPFPB-doped C_{60} powder. c) The XPS spectra of F1s, C1s, and B1s in the TPFPB film, 4 wt% TPFPB-doped C_{60} film, and pristine C_{60} film. d) The optimized molecular orbital graphs of the C_{60} and C_{60}·TPFPB complex. e) The UPS cutoff spectra of the C_{60} and 4 wt% TPFPB-doped C_{60} films. f) The TRPL spectra of the perovskite film with different ETLs. g) The dark *J–V* characteristics of the electron-only perovskite devices (FTO/ZnO/perovskite/ZnO@C_{60}/Ag) with and without incorporation of TPFPB.

capacitance–voltage (*C–V*) characterizations to elucidate the underlying physics of the V_{OC} improvement. The intercept with the *x*-axis can be associated to the built-in potential (V_{bi}) by Mott–Schottky analysis. The extracted V_{bi} increased from 0.95 V in the control device to 1.05 V in 4 wt% TPFPB-doped device (Figure S3, Supporting Information), which means that the TPFPB-doped ETL can facilitate charge separation and prevent carrier recombination.[43] However, we found that the TPFPB-doped inorganic $CsPbI_2Br$ suffered from severe hysteresis and it became more pronounced with increasing dopant concentration (Figure S4, Table S2, Supporting Information). In order to quantitatively evaluate the *J–V* hysteresis effect, we calculated the hysteresis index (*H*-index) with the equation of $H\text{-index} = (PCE_{RS} - PCE_{FS})/PCE_{RS}$, where the PCE_{RS} and PCE_{FS} represent the PCE from reverse scan (RS) and forward scan (FS), respectively.[44] The estimated *H*-index for the best performed device is ≈12.87% as depicted in Figure 1b, which is considered to be too large for a properly working PSC. As a result, the stabilized power output (SPO) displayed inferior PCE and declined rapidly from 13.3% to 12.7% within 150 s (Figure 1d).

We performed electrostatic potential (ESP) analysis by the density functional theory (DFT) method to explore the mechanism behind both improved PCE and induced hysteresis effect with respect to incorporation of TPFPB.[45] The molecular structures and calculated ESP images of C_{60} and TPFPB are displayed in **Figure 2**a. Both C_{60} and TPFPB have an electron-deficient area (positive area) as well as an electron-accepting area (negative area), which possibly provides a favorable condition for coordination with each other. In the C_{60} molecule, the negative areas are mainly distributed at the edges and vertexes, which shared by two adjacent rings, while the positive areas are mainly located above and below the center of the five-membered and six-membered rings.[46] Concomitantly, the positive areas in TPFPB are associated with fluorine, and the strongest negative area is located around the boron atom due to its vacant p orbit. It seems that the $C_{60}\cdot$TPFPB complex has two types of configurations: i) C—F$\cdots C_{60}$ configuration, in which one or more C—F bonds joint(s) to the five-membered or six-membered rings; ii) B$\cdots C_{60}$ configuration, in which the negative areas in C_{60} are attracted by boron atom in TPFPB. Nevertheless, we found the C—F$\cdots C_{60}$ configuration is not stable because the energy of the structure C—F$\cdots C_{60}$ is not at a minimum point. A more stable structure of $C_{60}\cdot$TPFPB complex with B$\cdots C_{60}$ configuration is illustrated in Figure 2a and the values of combining energies are listed in Table S3 (Supporting Information). The interaction is mainly dominated by dispersion and the total combining energy is –18.6 kcal mol^{-1}. The interaction between TPFPB and C_{60} molecule has been further verified by Fourier transform infrared (FTIR) spectroscopy measurements. As shown in Figure 2b, the peaks located at 526.6 and 576.0 cm^{-1} are corresponding to C_{60} molecule which has almost same wavenumbers after TPFPB doping, whereas the peaks located at 1647.4, 1519.0, and 1468.7 cm^{-1} that belong to the fluorinated benzene ring were shifted to lower wavenumbers. This can be explained by the rigid body of C_{60} and interaction effect between TPFPB and C_{60} molecule. In addition, the stretching vibration of C—B bond in TPFPB is shifted from 1103.6 cm^{-1} to lower wavenumber of 1084.9 and 1083.1 cm^{-1} for 20 wt% and 4 wt% of TPFPB-doped C_{60} samples, which indicates a decrement in bond strength between C and B due to the formation of coordination adduct.[47]

In order to further understand the interaction between C_{60} and TPFPB, X-ray photoelectron spectroscopy (XPS) have been performed. We investigated the peaks of F1s, C1s, and B1s in the XPS spectra (Figure 2c). It can be observed that the C1s peak from C_{60} is shifted toward higher binding energy while the F1s and B1s peaks belonging to the TPFPB are shifted to lower binding energy after the incorporation of TPFPB into C_{60} film, suggesting that the electron density around the boron atom was increased, due to the donation of electrons to the carbon atom.[21] Moreover, the HOMO and LUMO energy levels of C_{60} without or with TPFPB doping have been calculated to understand the changes of frontier electron orbitals, as the molecular orbital configurations are depicted in Figure 2d. The LUMO image of TPFPB-doped C_{60} intuitively exhibits less delocalization across the π-conjugated framework, which means that the electron density was withdrawn from the C_{60} and shifted to the TPFPB molecule. As a consequence, the obtained LUMO level is decreased from –3.22 to –3.34 eV with the attachment of TPFPB. Note that the calculated value of HOMO and LUMO are only used for internal comparison as the orbitals are one-electron approximations.

To verify the above simulation, the ultraviolet photoelectron spectroscopy (UPS) has been used to calculate the energy levels of TPFPB-doped C_{60} thin film. The measured HOMO levels of C_{60} with and without TPFPB are 21.22 eV – (19.94–5.12 eV) = 6.4 eV and 21.22 eV – (19.34–4.44 eV) = 6.32 eV, respectively. The bandgaps of the pristine C_{60} and TPFPB-doped C_{60} films are 1.79 and 1.80 eV, derived from the absorption spectra (Figure S5, Supporting Information). Thus, the calculated LUMO energy of the 4 wt% TPFPB-doped C_{60} film is 6.4–1.8 eV = 4.6 eV (LUMO = HOMO – E_g), which is 70 meV deeper than 4.53 eV (6.32–1.79 eV) of a pristine C_{60} film (Figure 2e). A deeper LUMO level of TPFPB-doped C_{60} allows to provide a larger free energy difference in efficient electron injection.[38] Time-resolved photoluminescence (TRPL) spectra have been conducted on the samples of glass/$CsPbI_2Br$ and glass/$CsPbI_2Br$/ETLs (ETLs: ZnO@C_{60}, ZnO@4 wt% TPFPB-doped C_{60}) to examine the electron extraction capabilities of corresponding ETL bilayers. Obviously, the bare perovskite thin film possesses the longest lifetime, and the ETL-containing samples show the reduced fluorescence lifetimes. The 4 wt% TPFPB-doped device has a shorter lifetime (1.76 ns) than the pristine C_{60}-based sample (4.47 ns) (Figure 2f), which indicates an enhancement in electron extraction capability of ZnO@C_{60} bilayer after the doping of TPFPB. In addition, the electron trap states of the electron-only devices before and after doping TPFPB have been compared (Figure 2g). Typical J–V curves with ohmic current region and trap-fill limited (TFL) current region have been observed. The electron trap densities n_e can be calculated by $n_e = (2V_{TFL}\varepsilon_r\varepsilon_0)/eL^2$, where V_{TFL} is the trap-fill limit voltage, L and ε_r are the thickness and relative dielectric constant of $CsPbI_2Br$ active layer, ε_0 is the vacuum permittivity, and e is the electron charge. The trap density is reduced from 2.72×10^{16} cm^{-3} to 2.33×10^{16} cm^{-3} upon incorporation of TPFPB.[32] Therefore, the improvement in V_{OC} through incorporation of TPFPB can be associated with the enhanced charge extraction effect and decreased trap states.

In order to further find out the reason that causes the anomalous hysteresis, conductive atom force microscopy (c-AFM) analysis has been carried out and a space-charge-limited current (SCLC) model has been applied to characterize the film conductivity and electron mobility.[48,49] According to the 2D tapping-mode height images, a different topographic morphology is observed after doping of TPFPB, as the root-mean-square (RMS) roughness is slightly increased from 0.68 nm of the C_{60} film to 1.24 nm for the 4 wt% TPFPB-doped C_{60} thin film (Figure S6a,b, Supporting Information). In addition, the c-AFM images exhibit a significant difference, as more blue area is observed in **Figure 3**a when compared to Figure 3b, which indicates the occurrence of a larger current flow in the pristine C_{60} thin film as compared with in the 4 wt% TPFPB-doped C_{60} thin film. The mean current is decreased from 100.30 to 95.39 pA after quantifying the current maps (Figure 3d,e), confirming the reduction in conductivity after the incorporation of TPFPB. The current–voltage response also shows the reduced slope for the TPFPB-doped device (Figure S7, Supporting Information), which is consistent with the results of the c-AFM current maps (Figure 3d,e). In addition, the electron mobility of C_{60} and 4 wt% TPFPB-doped C_{60} films have been evaluated by means of the SCLC model with the equation of $j = (9\mu\varepsilon_0\varepsilon_r V^2)/8L^3$, where μ is the electron carrier mobility, ε_0 is the vacuum permittivity, ε_r is the relative permittivity of C_{60}, V is the applied voltage, and L is the film thickness.[50] The mobility of the 4 wt% TPFPB-doped C_{60} film is reduced from 1.67 to 0.39 cm^2 V^{-1} s^{-1} (Figure S8, Supporting Information). It is well known that the C_{60} molecule has 60 delocalized π electrons and the transportation of electrons is generally related to the π conjugation. In this work, the hopping of the delocalized π electron may be hindered due to the interposition of TPFPB between adjacent C_{60} molecules, resulting in the decrease of electron mobility and conductivity. As a result, the charge transport may be slowed

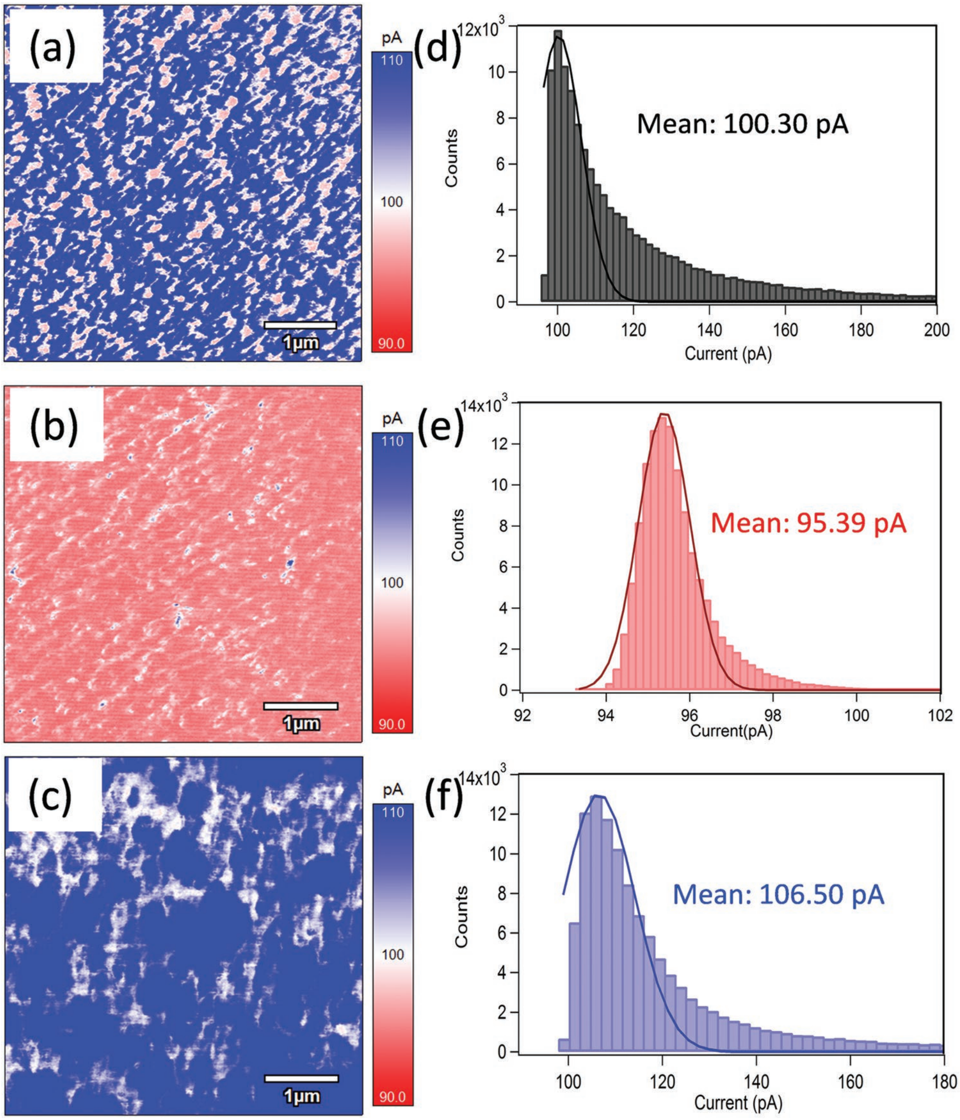

Figure 3. a–f) c-AFM images and quantized photocurrent statistics of C_{60} film (a,d), 4 wt% TPFPB-doped C_{60} film (b,e), and codoped C_{60} film (c,f).

down and cause charge accumulation, which is likely to be responsible for the pronounced hysteresis effect.

To suppress the negative effects of TPFPB doping and increase the electron mobility and conductivity at the same time, a controlled amount of lithium salt ($LiClO_4$) has been added into the TPFPB-doped C_{60} solution. The $LiClO_4$ has been used as the addictive for lithium salt instead of the widely used lithium bis(trifluoromethanesulfonyl)imide (LiTFSI) because of its less hygroscopic nature. As shown in Figure S9 (Supporting Information), LiTFSI powder changed into liquid within 45 min in air due to its strong hygroscopic nature, while the $LiClO_4$ powder possessed a negligible change when placed in air for more than 1 week (relative humidity: ≈70%). The electron mobility is increased from 0.39 to 1.21 $cm^2 V^{-1} s^{-1}$ (Figure S8, Supporting Information) as well as the quantified current from the c-AFM images is increased from 95.39 to 106.50 pA (Figure 3e,f) after the introduction of $LiClO_4$ into TPFPB-doped C_{60} film. The increase of slope of codoped device is also consistent with the results of c-AFM current images (Figure S7, Supporting Information). In addition, the Lewis acidic TPFPB also undergoes hydrophilic character, since water molecule can act as a Lewis base (Figure S10, Supporting Information),[51] which may reduce water resistance of the ETL capping bilayers. Fortunately, the ClO_4^- anions can coordinate with the dissociative TPFPB, which not only hinder the deliquescence of TPFPB, but also increase the film conductivity by releasing the Li^+ ions.[52] However, excessive $LiClO_4$ will weaken the effect between TPFPB and C_{60}, which make it necessary to optimize the dopant concentration of $LiClO_4$. Figure S11 (Supporting Information) shows the statistics of parameters of the PSCs with different $LiClO_4$ dopant concentrations into the C_{60} layer. All solar cell parameters are improved to some extent as the dopant concentration is increased, and the optimal performance is obtained with a dopant concentration of 0.1 wt%. Subsequently, the TPFPB and $LiClO_4$ codoped PSCs are fabricated. **Figure 4**a and

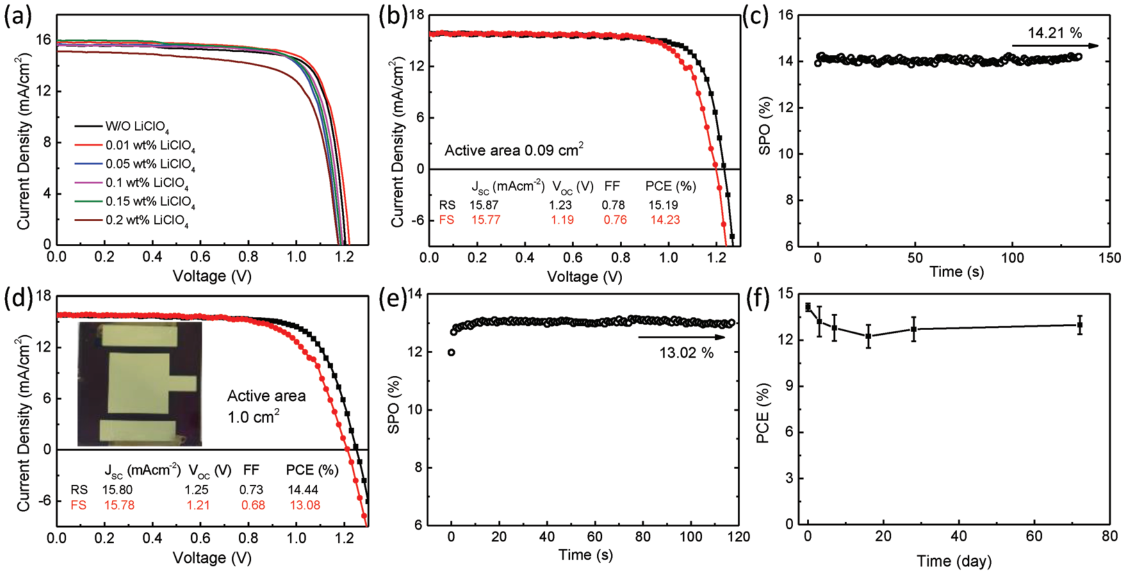

Figure 4. a) Typical *J–V* curves of inorganic $CsPbI_2Br$ PSCs with fixed 4 wt% TPFPB additive and varying dopant concentrations of $LiClO_4$. b) The *J–V* characteristics of the best performed inorganic $CsPbI_2Br$ PSC obtained in 4 wt% TPFPB and 0.01 wt% $LiClO_4$ codoped C_{60} condition. c) SPO measurement as a function of time held at 0.95 V forward bias. d) The *J–V* curves of the best performed large-area PSC; inset is the corresponding photograph of PSC with electrode area of 1.1 × 1.1 cm^2. e) The SPO measurement as a function of time held at 0.9 V forward bias. f) Long-term storage stability of the large-area PSCs (stored in nitrogen environment and tested in air).

Table S4 (Supporting Information) respectively exhibit the typical *J–V* curves and parameters of inorganic $CsPbI_2Br$ PSCs with fixed 4 wt% TPFPB additive and varying dopant concentrations of $LiClO_4$. The best solar cell is obtained at the $LiClO_4$ dopant concentration of 0.01 wt%, while higher dopant concentration leads to a decrease in V_{OC}, which can be related to weakened coordination effect between TPFPB and C_{60}. Finally, a champion PCE of 15.19% (RS) is achieved after repeated optimization with V_{OC} of 1.23 V, J_{SC} of 15.87 mA cm^{-2}, and FF of 0.78. Additionally, the PCE obtained from forward scan is 14.23% with V_{OC} of 1.19 V, J_{SC} of 15.77 mA cm^{-2}, and FF of 0.76 (Figure 4b). Encouragingly, the *H*-index is reduced to ≈6.32%, which is significantly less than that of single TPFPB-doped PSC as well as control PSC. The corresponding SPO performance has been recorded at a forward bias of 0.95 V and achieved a stabilized PCE of 14.21% without obvious decline (Figure 4c). The EQE spectrum and the corresponding integral current density as a function of wavelength are shown in Figure S12 (Supporting Information) with integrated current density of 15.1 mA cm^{-2}. Statistics of photovoltaic parameters of PSCs fabricated with pristine and doped C_{60} ETLs is shown in Figure S13 (Supporting Information), indicating a good repeatability. A square-centimeter area (1.0 cm^2) PSC has also been fabricated and a high PCE of 14.44% has been obtained (Figure 4d), which is the highest PCE reported for inorganic $CsPbI_2Br$ PSC with an active area of ≈1.0 cm^2 as far as we know (Figure S1b, Supporting Information). Interestingly, the large-area device showed a V_{OC} of 1.25 V, which is 20 mV larger than the PSCs with small area. The corresponding SPO performance has been recorded at a forward bias of 0.95 V around the maximum power point and achieved a stabilized PCE of 13.02% within 120 s (Figure 4e). Subsequently, the storage stability of the large-area PSCs has been monitored. The devices without any encapsulation still retain about ≈91.8% of its initial PCE after being tracked for 72 d (Figure 4f).

As mentioned above, the incorporation of $LiClO_4$ is beneficial in that it weakens the hygroscopicity of TPFPB, which is expected to improve the humidity stability of the PSCs. Figure S14 (Supporting Information) shows the water contact angle measurements carried out on the devices FTO/NiO_x/perovskite/ZnO@C_{60} (TPFPB-doped C_{60} or TPFPB + $LiClO_4$ codoped C_{60}). The water contact angle is decreased from 118.5° to 110.5° after the incorporation of 4 wt% TPFPB and then increased to 114° with sequentially addition of 0.01 wt% $LiClO_4$. These results suggest that the enhanced surface energy of the ETLs upon introduction of $LiClO_4$ can improve the moisture resistance of inorganic PSCs. Thus, thermal stability measurements of the PSCs (Au electrode) with and without dopant have been conducted at 60 °C both in air and in N_2 environment. As can be seen in Figure S15 (Supporting Information), the control devices possessed the most stable performance with nearly no decline within 23 h, which is consistent with our previous report.[30] At the same time, the TPFPB-doped device exhibits the fastest decline as the PCE decreases by half within 8 h. In comparison, the codoped $CsPbI_2Br$ PSC still maintains 70% of its initial PCE after being heated in air for 19 h (Figure S15, Supporting Information). In order to visualize different degradation behaviors of the corresponding PSCs, the photographs are displayed in Figure S16 (Supporting Information). Negligible changes are observed for the control device after 23 h annealing in air whereas a severe degradation is observed for TPFPB-doped device just after 4 h of annealing. Concomitantly, the codoped device began to degrade after 10 h, which indicates its increased stability when compared to TPFPB-doped PSCs. In contrast, the TPFPB-doped PSCs display about 10% decline of their initial PCE after being heated at 60 °C in N_2 for 132 h (Figure S17, Supporting Information). The PCE of codoped devices increased slightly in the first 12 h of heating, which can be attributed to the decreased trap-state density and improved interface charge-transfer properties.[31] Subsequently, the thermal stability of the codoped devices exhibited about 15% decline after heated for 132 h when compared with their initial PCE. We further tracked the long-term 1 sun light soaking lifetime of the PSCs. As shown in Figure S18 (Supporting Information), the PCE of the control and the codoped devices increase slightly in the first 24 h of light illumination, which can be attributed to the light-induced defect healing effect in the PSC.[53] Subsequently, the efficiency begins to decline, but the PCEs are retained (codoped devices) or higher (control devices) than the initial PCEs after 132 h of light illumination. In contrast, the TPFPB-doped devices display a fast decline of PCE with about 30% decline of its initial PCE when aging for 132 h under light illumination in N_2. These results indicate that TPFPB-doped devices are more sensitive to humidity in the air and to light illumination, and the codoped device is assumed to be a compromise between efficiency and stability.

We further fabricated an inorganic perovskite solar module with 4 subcells connected in series (**Figure 5**c). However, with the increase of substrate size (from 2.5 × 2.5 cm^2 to 5 × 5 cm^2), the phase transition process at the center region will lag far behind the edge region (Figure 5b_1), resulting in nonuniform perovskite film (Figure S19a,c, Supporting Information). To solve this problem, we have upgraded the thermal radiant heating method (TRHM)[30] by placing a curved glass under the sample substrate to form a quasi-curved heating surface of hotplate (Figure 5a). The heated curved glass accelerates the phase transition of the center region so that the whole substrate can undergo the phase transition process at the same time (Figure 5b_2), thus ensuring the uniformity of the perovskite film (Figure S19b,d, Supporting Information). We name this upgraded method as the quasi-curved hotplate thermal radiation heating method (for short: quasi-curved heating method). The thermal infrared videos (Supporting Information) were applied to in suit monitor the distribution of the heat field during the phase transition heating process. The area of each subcell is 0.75 × 4.4 cm^2 and each dead area is 0.25 × 4.4 cm^2, leading to geometric fill factor of

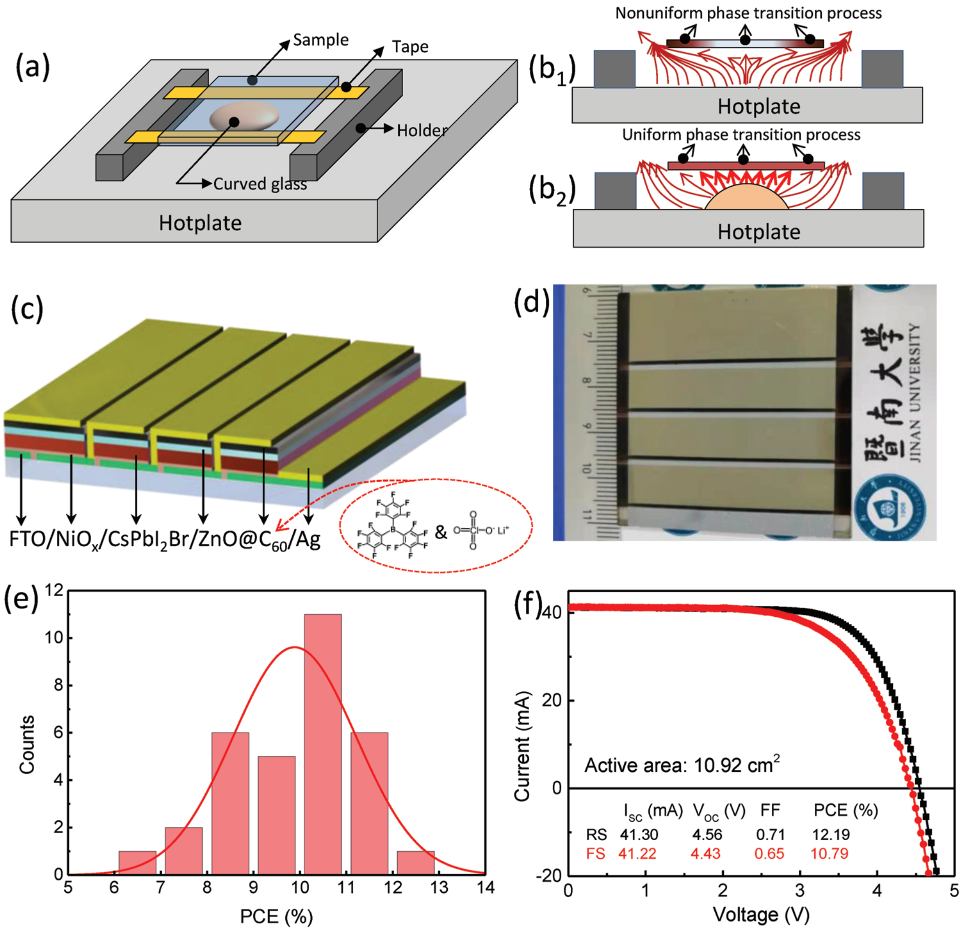

Figure 5. a) Schematic view of quasi-curved heating method to fabricate $CsPbI_2Br$ thin film on large substrate. b) Side view to understand the changes in thermal radiation patterns after placing the curved glass under the sample substrate. c) A schematic diagram of inorganic perovskite solar module with four subcells connected in series. d) Photograph of the inorganic $CsPbI_2Br$ perovskite solar module. e) Statistical histogram of the PCE of $CsPbI_2Br$ perovskite solar modules, represented for 32 data points. f) The *J–V* characteristics of the best-performing $CsPbI_2Br$ perovskite solar module.

75% (Figure S20a, Supporting Information).[12] The size of each mask is 0.65×4.2 cm^2, giving the total active area of the module of 10.92 cm^2 (Figure S20b, Supporting Information). The photograph of as-fabricated inorganic perovskite solar module was shown in Figure 5d and Figure S21 (Supporting Information). We optimized the thickness of the ZnO layer, as the typical J–V curves are shown in Figure S22a (Supporting Information). Compared with solar cells, the solar module needs a thicker ZnO layer to avoid leakage loss (Figure S22b, Supporting Information) due to the inherent unevenness of the spin coating applied to a large substrate. Subsequently, 32 solar modules were fabricated and their parameters were statistically calculated (Figure 5e and Figure S23, Supporting Information). Inspiringly, the solar modules show low performance loss compared with the solar cells, which leads to the best-performing solar module showing a PCE of 12.19% (I_{SC} = 41.30 mA, V_{OC} = 4.56 V, and FF = 0.71) (Figure 5f). To the best of our knowledge, this is the first solar module reported with inorganic perovskite absorber. In addition, the inorganic solar module without any encapsulation can retain about ≈86.5% of its initial PCE after being stored for 75 d in nitrogen atmosphere (Figure S24, Supporting Information).

In conclusion, our work demonstrated significant improvements in V_{OC} and overall photovoltaic performances of inorganic $CsPbI_2Br$ PSCs by tailoring of C_{60} via our codoping strategy. Theoretical calculations and experimental measurements including FTIR and XPS were applied to verify the coordination between Lewis acid TPFPB dopant and C_{60}. The Lewis acid TPFPB molecule attracts the electrons from the C_{60} molecule, resulting in an occurrence of a lower LUMO level of C_{60}. TRPL spectra demonstrated enhanced electron extraction ability, and the characterization of trap states indicated a reduced electron trap density. The as-fabricated inverted inorganic $CsPbI_2Br$ PSC with TPFPB-doped C_{60} yielded a V_{OC} as high as 1.23 V, which is much larger than that of the PSCs with pristine C_{60}. However, the hysteresis effect became more pronounced with increasing dopant concentration of TPFPB. The severe hysteresis can be ascribed to the decrement in electron mobility and conductivity, due to the formation of a $C_{60}\cdot$TPFPB complex that inhibits the hopping of the delocalized π electron within the ETL. Subsequently, the introduction of a certain amount of $LiClO_4$ enhanced the conductivity of film as well as the humidity stability and light illumination stability. The as-optimized inorganic PSCs with codoped C_{60} ETL showed a champion PCE of 15.19% (stabilized efficiency of 14.21%) with acceptable J–V hysteresis for a small-area (0.09 cm^2) device. Nevertheless, we believe that further work is needed to eliminate the hysteresis effects especially on the optimization of the inorganic perovskite material. Furthermore, a high PCE of 14.44% was obtained for a large-area device with square centimeter active layer, which is the highest PCE reported for an inorganic PSC with an area of 1.0 cm^2. The large-area PSCs retained ≈91.8% of their initial PCE after having been stored for 72 d. More importantly, for the first time, an inorganic perovskite solar module as obtained by the quasi-curved heating method is reported with an efficiency exceeding 12% (10.92 cm^2). We believe that this present work can provide a facile approach toward the fabrication of high-efficiency, inorganic $CsPbI_2Br$ PSCs with low hysteresis and may make the fabrication of larger area inorganic perovskite solar modules feasible.

Supporting Information

Supporting Information is available from the Wiley Online Library or from the author.

Acknowledgements

This work was supported by the National Key R&D Program of China (Grant No. 2018YFB1500103 and 2016YFA0201001), "Advanced Talents Program of Hebei Province" (No. GCC2014013). The authors also thank Yumiao Ma from Shiyanjia lab for the ESP analysis (www.shiyanjia.com).

Conflict of Interest

The authors declare no conflict of interest.

Keywords

high efficiency, inorganic perovskite solar cells, large area, modules, uniform

Received: November 9, 2019
Revised: December 6, 2019

---

[1] S. Yang, J. Dai, Z. Yu, Y. Shao, Y. Zhou, X. Xiao, X. C. Zeng, J. Huang, *J. Am. Chem. Soc.* **2019**, *141*, 5781.
[2] A. Polman, M. Knight, E. C. Garnett, B. Ehrler, W. C. Sinke, *Science* **2016**, *352*, aad4424.
[3] A. Kojima, K. Teshima, Y. Shirai, T. Miyasaka, *J. Am. Chem. Soc.* **2009**, *131*, 6050.
[4] J. Burschka, N. Pellet, S. J. Moon, R. Humphry-Baker, P. Gao, M. K. Nazeeruddin, M. Gratzel, *Nature* **2013**, *499*, 316.
[5] M. Liu, M. B. Johnston, H. J. Snaith, *Nature* **2013**, *501*, 395.
[6] W. S. Yang, J. H. Noh, N. J. Jeon, Y. C. Kim, S. Ryu, J. Seo, S. I. Seok, *Science* **2015**, *348*, 1234.
[7] Q. Jiang, Y. Zhao, X. Zhang, X. Yang, Y. Chen, Z. Chu, Q. Ye, X. Li, Z. Yin, J. You, *Nat. Photonics* **2019**, *13*, 460.
[8] NREL best research cell efficiencies, https://www.nrel.gov/pv/assets/pdfs/best-research-cell-efficiencies.20190802.pdf (accessed: August 2019).
[9] D. Wang, M. Wright, N. K. Elumalai, A. Uddin, *Sol. Energy Mater. Sol. Cells* **2016**, *147*, 255.
[10] M. Konstantakou, T. Stergiopoulos, *J. Mater. Chem. A* **2017**, *5*, 11518.
[11] Y. Hu, S. Si, A. Mei, Y. Rong, H. Liu, X. Li, H. Han, *Sol. RRL* **2017**, *1*, 1600019.
[12] F. Guo, S. Qiu, J. Hu, H. Wang, B. Cai, J. Li, X. Yuan, X. Liu, K. Forberich, C. J. Brabec, Y. Mai, *Adv. Sci.* **2019**, *6*, 1901067.
[13] J. Liang, C. Wang, Y. Wang, Z. Xu, Z. Lu, Y. Ma, H. Zhu, Y. Hu, C. Xiao, X. Yi, G. Zhu, H. Lv, L. Ma, T. Chen, Z. Tie, Z. Jin, J. Liu, *J. Am. Chem. Soc.* **2016**, *138*, 15829.
[14] C. Liu, W. Li, C. Zhang, Y. Ma, J. Fan, Y. Mai, *J. Am. Chem. Soc.* **2018**, *140*, 3825.
[15] R. J. Sutton, G. E. Eperon, L. Miranda, E. S. Parrott, B. A. Kamino, J. B. Patel, M. T. Hörantner, M. B. Johnston, A. A. Haghighirad, D. T. Moore, H. J. Snaith, *Adv. Energy Mater.* **2016**, *6*, 1502458.
[16] G. E. Eperon, G. M. Paternò, R. J. Sutton, A. Zampetti, A. A. Haghighirad, F. Cacialli, H. J. Snaith, *J. Mater. Chem. A* **2015**, *3*, 19688.
[17] H. Wang, H. Bian, Z. Jin, H. Zhang, L. Liang, J. Wen, Q. Wang, L. Ding, S. F. Liu, *Chem. Mater.* **2019**, *31*, 6231.

[18] Y. Wang, M. I. Dar, L. K. Ono, T. Zhang, M. Kan, Y. Li, L. Zhang, X. Wang, Y. Yang, X. Gao, Y. Qi, M. Gratzel, Y. Zhao, *Science* **2019**, *365*, 591.
[19] Y. Wang, T. Zhang, M. Kan, Y. Zhao, *J. Am. Chem. Soc.* **2018**, *140*, 12345.
[20] P. Wang, X. Zhang, Y. Zhou, Q. Jiang, Q. Ye, Z. Chu, X. Li, X. Yang, Z. Yin, J. You, *Nat. Commun.* **2018**, *9*, 2225.
[21] J. Tian, Q. Xue, X. Tang, Y. Chen, N. Li, Z. Hu, T. Shi, X. Wang, F. Huang, C. J. Brabec, H. L. Yip, Y. Cao, *Adv. Mater.* **2019**, *31*, e1901152.
[22] W. Chen, H. Chen, G. Xu, R. Xue, S. Wang, Y. Li, Y. Li, *Joule* **2019**, *3*, 191.
[23] J. Duan, Y. Zhao, B. He, Q. Tang, *Angew. Chem., Int. Ed.* **2018**, *57*, 3787.
[24] Y. Zhang, C. Wu, D. Wang, Z. Zhang, X. Qi, N. Zhu, G. Liu, X. Li, H. Hu, Z. Chen, L. Xiao, B. Qu, *Sol. RRL* **2019**, *3*, 1900254.
[25] C. Y. Chen, H. Y. Lin, K. M. Chiang, W. L. Tsai, Y. C. Huang, C. S. Tsao, H. W. Lin, *Adv. Mater.* **2017**, *29*, 1605290.
[26] C. Liu, W. Li, J. Chen, J. Fan, Y. Mai, R. E. I. Schropp, *Nano Energy* **2017**, *41*, 75.
[27] S. Zhang, W. Chen, S. Wu, R. Chen, Y. Huang, Z. Yang, J. Li, L. Han, W. Chen, *J. Mater. Chem. A* **2019**, *7*, 18603.
[28] D. Han, Y. Xin, Q. Yuan, Q. Yang, Y. Wang, Y. Yang, S. Yi, D. Zhou, L. Feng, Y. Wang, *Sol. RRL* **2019**, *3*, 1900091.
[29] S. Zhang, S. Wu, W. Chen, H. Zhu, Z. Xiong, Z. Yang, C. Chen, R. Chen, L. Han, W. Chen, *Mater. Today Energy* **2018**, *8*, 125.
[30] C. Liu, W. Li, H. Li, H. Wang, C. Zhang, Y. Yang, X. Gao, Q. Xue, H.-L. Yip, J. Fan, R. E. I. Schropp, Y. Mai, *Adv. Energy Mater.* **2019**, *9*, 1803572.
[31] X. Liu, Y. Xiao, Q. Zeng, J. Jiang, Y. Li, *J. Phys. Chem. Lett.* **2019**, *10*, 6382.
[32] G. Yin, H. Zhao, H. Jiang, S. Yuan, T. Niu, K. Zhao, Z. Liu, S. F. Liu, *Adv. Funct. Mater.* **2018**, *28*, 1803269.
[33] S. S. Mali, J. V. Patil, C. K. Hong, *Nano Lett.* **2019**, *19*, 6213.
[34] Y. Fan, J. Fang, X. Chang, M.-C. Tang, D. Barrit, Z. Xu, Z. Jiang, J. Wen, H. Zhao, T. Niu, D.-M. Smilgies, S. Jin, Z. liu, E. Q. Li, A. Amassian, S. F. Liu, K. Zhao, *Joule* **2019**, *3*, 2485.
[35] T. Niu, J. Lu, R. Munir, J. Li, D. Barrit, X. Zhang, H. Hu, Z. Yang, A. Amassian, K. Zhao, S. F. Liu, *Adv. Mater.* **2018**, *30*, 1706576.
[36] Y. Shao, Y. Yuan, J. Huang, *Nat. Energy* **2016**, *1*, 15001.
[37] Q. Jiang, L. Zhang, H. Wang, X. Yang, J. Meng, H. Liu, Z. Yin, J. Wu, X. Zhang, J. You, *Nat. Energy* **2016**, *2*, 16177.
[38] X. Gong, Q. Sun, S. Liu, P. Liao, Y. Shen, C. Gratzel, S. M. Zakeeruddin, M. Gratzel, M. Wang, *Nano Lett.* **2018**, *18*, 3969.
[39] L. Yan, Q. Xue, M. Liu, Z. Zhu, J. Tian, Z. Li, Z. Chen, Z. Chen, H. Yan, H. L. Yip, Y. Cao, *Adv. Mater.* **2018**, *30*, e1802509.
[40] E. V. Anslyn, D. A. Dougherty, *Modern Physical Organic Chemistry*, University Science Books, Sausalito, CA, USA **2006**.
[41] H. Yan, J. Chen, K. Zhou, Y. Tang, X. Meng, X. Xu, W. Ma, *Adv. Energy Mater.* **2018**, *8*, 1703672.
[42] J. Luo, J. Xia, H. Yang, L. Chen, Z. Wan, F. Han, H. A. Malik, X. Zhu, C. Jia, *Energy Environ. Sci.* **2018**, *11*, 2035.
[43] D. Bai, J. Zhang, Z. Jin, H. Bian, K. Wang, H. Wang, L. Liang, Q. Wang, S. F. Liu, *ACS Energy Lett.* **2018**, *3*, 970.
[44] Q. Jiang, Z. Chu, P. Wang, X. Yang, H. Liu, Y. Wang, Z. Yin, J. Wu, X. Zhang, J. You, *Adv. Mater.* **2017**, *29*, 1703811.
[45] T. Wu, Y. Wang, Z. Dai, D. Cui, T. Wang, X. Meng, E. Bi, X. Yang, L. Han, *Adv. Mater.* **2019**, *31*, e1900605.
[46] M. M. Li, Y. B. Wang, Y. Zhang, W. Wang, *J. Phys. Chem. A* **2016**, *120*, 5766.
[47] N. Ahn, D. Y. Son, I. H. Jang, S. M. Kang, M. Choi, N. G. Park, *J. Am. Chem. Soc.* **2015**, *137*, 8696.
[48] J. Li, B. Huang, E. N. Esfahani, L. Wei, J. Yao, J. Zhao, W. Chen, *npj Quantum Mater.* **2017**, *2*, 56.
[49] G. Xia, B. Huang, Y. Zhang, X. Zhao, C. Wang, C. Jia, J. Zhao, W. Chen, J. Li, *Adv. Mater.* **2019**, *31*, 1902870.
[50] M. Chen, M. G. Ju, H. F. Garces, A. D. Carl, L. K. Ono, Z. Hawash, Y. Zhang, T. Shen, Y. Qi, R. L. Grimm, D. Pacifici, X. C. Zeng, Y. Zhou, N. P. Padture, *Nat. Commun.* **2019**, *10*, 16.
[51] S. Wang, Z. Huang, X. Wang, Y. Li, M. Gunther, S. Valenzuela, P. Parikh, A. Cabreros, W. Xiong, Y. S. Meng, *J. Am. Chem. Soc.* **2018**, *140*, 16720.
[52] H. Lee, X. Yang, C. Xiang, J. McBreen, L. Choi, *J. Electrochem. Soc.* **1998**, *145*, 2813.
[53] R. Lin, K. Xiao, Z. Qin, Q. Han, C. Zhang, M. Wei, M. I. Saidaminov, Y. Gao, J. Xu, M. Xiao, A. Li, J. Zhu, E. H. Sargent, H. Tan, *Nat. Energy* **2019**, *4*, 864.